



Cite this: *Phys. Chem. Chem. Phys.*,
2018, 20, 10319

Multiple conical intersections in small linear parameter Jahn–Teller systems: the DMBE potential energy surface of ground-state C_3 revisited[†]

C. M. R. Rocha and A. J. C. Varandas *

A new single-sheeted DMBE potential energy surface for ground-state C_3 is reported. The novel analytical form accurately describes the three symmetry-equivalent C_{2v} disjoint seams, in addition to the symmetry-required D_{3h} one, over the entire configuration space. The present formalism warrants by built-in construction the confluence of the above crossings, and the rotation-in-plane of the C_{2v} seams when the perimeter of the molecule fluctuates. Up to 1050 *ab initio* energies have been employed in the calibration procedure, of which 421 map the loci of intersection. The calculated energies have been scaled to account for the incompleteness of the basis set and truncation of the MRCI expansion, and fitted analytically with chemical accuracy. The novel form is shown to accurately mimic the region defined by the 4 conical intersections, while exhibiting similar attributes to the previously reported one [*J. Chem. Phys.*, 2015, **143**, 074302] at the regions of configuration space away from the crossing seams. Despite being mainly addressed to C_3 , the present approach should be applicable to adiabatic PESs of any X_3 system experiencing similar topological attributes, in particular the small-linear-parameter Jahn–Teller molecules.

Received 28th September 2017,
Accepted 13th March 2018

DOI: 10.1039/c7cp06656b

rsc.li/pccp

1 Introduction

Conical intersections (Cis) form hyperlines in the nuclear configuration space where two (or more) adiabatic potential energy surfaces (PESs) are degenerate.¹ Such hyperlines are referred to as seams (or locus) of Cis. Their orthogonal complements define the so-called branching² or (g,h) -plane³ at which degeneracies are linearly lifted in displacements from the intersection, assuming a local topology of a double cone.⁴ Conventionally, degeneracies on PESs are classified as normal (or symmetry-required) when they are naturally dictated by the molecular point group [as in the Jahn–Teller (JT) case^{5–9}] and accidental.^{1,3,10} These include both symmetry-allowed Cis (if the symmetries of the involved states carry distinct one-dimensional irreducible representations) and degeneracies involving two states of the same symmetry, which can only occur when two independent conditions are satisfied.^{11–14} Although often considered a theoretical curiosity, the conditions for electronic degeneracies have long been recognized by von Neumann and Wigner,¹¹ with Teller¹² emphasizing 80 years ago their role in fast radiationless transitions. Rather than the “non-crossing rule”,^{11–14}

Herzberg and Longuet-Higgins¹³ and Longuet-Higgins¹⁴ have shown that intersections of PESs are possible in systems with the same spin and spatial symmetries as long as they involve 2 or more configurational degrees of freedom. When dictated by symmetry, Jahn and Teller⁵ demonstrated that the very nature of Cis relies on the molecular point groups, thus occurring whenever two electronic states (at highly symmetric non-linear arrangements) transform as twofold degenerate irreducible representations.⁵ Cis lie also at the heart of nonadiabatic processes^{1,10} and related phenomena associated with the so-called geometric phase (GP) effect.^{13–16}

Regardless of the nature of Cis, they make the task of modeling an accurate global PES increasingly cumbersome. This is so, since standard analytic functions are inappropriate to describe the characteristic cusp behavior of the involved electronic states in the vicinity of the degeneracy seam.^{17,18} Given the divergent nature of the nonadiabatic coupling terms (NACTs) and the pronounced electronic interstate couplings [the breakdown of the Born–Oppenheimer (BO) approximation^{19,20}] at the locus of intersection and immediacies,¹ one could then resort to appropriate diabatization schemes.^{21–30} By employing an adiabatic-to-diabatic (ATD) unitary transformation so that the leading terms of the NACTs are partially removed, the diagonal adiabatic PESs (strictly speaking, *ab initio* energies) are replaced by a potential matrix whose elements are smooth functions of the

Departamento de Química, and Centro de Química, Universidade de Coimbra,
3004-535 Coimbra, Portugal. E-mail: varandas@uc.pt

† Electronic supplementary information (ESI) available. See DOI: 10.1039/c7cp06656b

nuclear coordinates.^{22,27–30} Such diabatic states, once properly obtained and conveniently modeled by some smooth functional forms, can be back transformed to adiabatic ones, therefore yielding the expected cusp behavior in the vicinity of the crossing seams. Despite its advantages, the resolution in terms of diabatic basis is nontrivial and, together with the need for a proper modeling of the potential matrix, makes the process of obtaining accurate global PESs increasingly complex.^{17,18} Actually, for molecules other than diatomics, strictly diabatic bases that exactly diagonalize the nuclear kinetic energy operators do not exist²¹ and hence, any attempt to minimize NACTs often leads to arbitrariness in the construction of the (quasi)-diabatic states.^{21,23–26}

Another possibility to describe a cusp on adiabatic PESs has been proposed by Varandas and Murrell.³¹ The authors employed the so-called JT-type coordinate^{31,32} ($\sqrt{T_2}$) together with suitable additional polynomial terms to introduce the required nonanalyticity into the adiabatic PESs of $H_3(1^2A')$, which shows the symmetry-required Cis for D_{3h} arrangements.^{31,33} Indeed, $\sqrt{T_2}$ has been especially designed to model adiabatic PESs of X_3 -type JT molecules in which a doubly degenerate pair of electronic states (E) is coupled by a doubly degenerate normal mode (e) [the well-studied linear $E \otimes e$ JT systems^{2–4,6–9}]. As such, the approach has been successfully applied to model accurate global PESs for ref. 34–36 $H_3^+(1^3A'/2^3A')$ and ref. 37 $N_3(1^2A''/2^2A'')$ molecules without the need of any ATD transformation. As stated in ref. 17, the JT coordinate is simply the distance from a given point in the branching plane³ to the corresponding origin (the D_{3h} crossing seam) and hence ensures, by built-in construction, the correct linear dependence of the potential (the conical shape) along the non-totally symmetric distortions.^{31,32,34–37}

Recently, Galvão, Mota and Varandas (GMV)^{17,18} extended the above methodology to include cusps on adiabatic single-sheeted PESs of any triatomic system exhibiting accidental Cis.¹⁷ Such an approach relies on finding the appropriate parametric equation that characterizes the locus of intersection and, from simple geometric considerations, defines the distance from any point in \mathbf{R} -space to the seam.^{17,18} The GMV scheme has been employed to accurately model the C_{2v} degeneracy line ($^2A_2/ ^2B_1$) of ref. 38 and 39 $NO_2(1^2A'')$ as well as the three permutationally equivalent seams of ref. 30 $N_3(1^2A')$. Further progress on the methodology has recently been reported.¹⁸ The authors suggested the use of a generalized JT-type coordinate (A) to mimic the desired singularities on the PESs of any triatomic system, including molecules having strongly curved (accidental) seams, as is the case of ref. 18, 27 and 40 $HN_2(1^2A')$; the reader is addressed to ref. 17 and 18 for details.

For general X_3 -type JT molecules, it is widely known that the introduction of quadratic terms in the vibronic coupling perturbation operator (the linear plus quadratic $E \otimes e$ problem^{6–9}) reveals the so-called warping of the Mexican-hat-type PESs with the formation of three-equivalent minima connected by three pseudo-rotation saddle points along the bottom of the “tricorn”.^{7–9} Yet, for molecules with small linear (F_E) and large quadratic (G_E) vibronic coupling constants, the locus of Cis and

hence the topology of the PESs near equilateral triangular arrangements is rather intricate.^{41,42} For such systems, referred to as small linear parameter (SLP) JT molecules,^{6,41–43} besides the usual symmetry-required D_{3h} seam, three additional symmetry-allowed Cis along the line of the C_{2v} symmetry are found in quite close proximity to the D_{3h} one. Such unusual topological features have been reported in the literature for elemental clusters such as $Li_3(2^2E')$,⁴⁴ $Na_3(2^2E')$,^{43,45,46} $K_3(2^2E')$,⁴⁷ $Si_3(1^1E')$,⁴⁸ $N_3^+(1^1E'')$,⁴⁹ and $C_3(1^1E')$.^{50,51} It is worth noting that, in addition to the proper JT effect,^{5–9} the presence of close-in-energy A states near the D_{3h} conformations is ubiquitous,^{44–51} so the overall problem at hand is effectively a three state one, *i.e.*, a combined JT plus pseudo-JT (PJT) case.^{48,50,51}

In previous work,⁵⁰ we have reported a single-sheeted DMBE PES (hereafter referred to as DMBE I) for ground-state $C_3(1^1A')$. There, we first outlined the presence of the 4 Cis characteristic of SLP JT systems. Because a third electronic state of $^1A'$ symmetry ($^1A'_1$ in D_{3h}) comes close in energy to the pair of intersecting states ($1^1E'$ in D_{3h}) near equilateral triangular arrangements,⁵¹ such unusual topological attributes have been ascribed to combined JT plus PJT vibronic effects.⁵⁰ Modeling of the D_{3h} and C_{2v} seams has then been accomplished by employing the JT coordinate and the GMV approach, respectively, along with suitable additional polynomial terms.⁵⁰ Since the term responsible for introducing the required singularities at C_{2v} degeneracies dies off Gaussian-like,¹⁷ the cusps are warranted only near the region defined by the minimum energy crossing point (MeX).⁵⁰ Note that these MeXs (including the one with D_{3h} symmetry) are minima along the A_1 totally symmetric coordinate (with continuous derivatives of the energy defined to any order along such a direction) but show discontinuities when traversing those crossing loci along the directions that split the degeneracy.

Most recently, the combined JT plus PJT $\left[\left(E' + A'_1\right) \otimes e'\right]$ problem in C_3 has been further exploited⁵¹ with somewhat unexpected results. Accordingly, the three additional symmetry-allowed C_{2v} seams are not static objects with respect to the symmetry-required (D_{3h}) one but evolve in location with varying perimeters of the molecule. In so doing, such degeneracy points approach the central D_{3h} Ci almost linearly and ultimately coalesce with it forming an intersection node⁵² or confluence.^{53,54} Additionally, by increasing the size of the molecular triangle, the C_{2v} disjoint seams get rotated by $\pm\pi$ in the branching plane.⁵¹ We have also proposed a three-state vibronic Hamiltonian that, once diagonalized, naturally mimics the 4 singularity points near the MeX of D_{3h} and C_{2v} symmetries as well as highlighted the implications of such multiple Cis on the net GP effect.

Our aim in this work is to devise a form (DMBE II) capable of accurately modeling the three symmetry-equivalent C_{2v} disjoint seams, in addition to the seam of D_{3h} symmetry, over the entire range of nuclear configuration space. Special attention is paid to developing a form that warrants by built-in construction the confluence of the above crossings and the rotation in the branching plane of the C_{2v} seams as the perimeter of the

molecule fluctuates. The approach that follows the original formalism should in principle be applicable to other cusps of any X_3 -type SLP JT system without the need of diabatization.

The paper is organized as follows. Section 2 summarizes the *ab initio* calculations. The strategy and analytical forms used in the DMBE I PES are briefly reviewed in Section 3. In Section 4, we devise an alternative scheme capable of accurately mimicking the symmetry-related C_{2v} seams over the entire configuration space, while in Section 5 the approach is used to get the DMBE II form. The major topological features of the current PES are discussed in Section 6 whereas Section 7 gathers the conclusions.

2 Ab initio calculations

All calculations have been performed at the multireference configuration interaction (MRCI) level using the full-valence complete active space self-consistent field [CASSCF(12,12) or FVCAS] wave functions as in ref. 55. The triple- ζ augmented correlation consistent basis set of Dunning^{56,57} (aug-cc-pVTZ or AVTZ) has been employed, and the calculations were done with MOLPRO.⁵⁸ To account for the incompleteness of the one- and N -electron bases, all raw *ab initio* energies have been scaled using the double many-body expansion-scaled external correlation (DMBE-SEC)⁵⁹ method, a methodology also utilized in ref. 50. All computations have been performed by considering cuts of the PES along the symmetry-adapted coordinates [$\mathbf{Q} = (Q_1, Q_2, Q_3)$] defined by^{22,60}

$$\begin{pmatrix} Q_1 \\ Q_2 \\ Q_3 \end{pmatrix} = \begin{pmatrix} \sqrt{1/3} & \sqrt{1/3} & \sqrt{1/3} \\ 0 & \sqrt{1/2} & -\sqrt{1/2} \\ \sqrt{2/3} & -\sqrt{1/6} & -\sqrt{1/6} \end{pmatrix} \begin{pmatrix} R_1 \\ R_2 \\ R_3 \end{pmatrix}, \quad (1)$$

where Q_1 is related to the perimeter of the triatomic system, and the pair (Q_2, Q_3) defines the shape of the molecular triangle; $\mathbf{R} = (R_1, R_2$ and $R_3)$ are internuclear distances.⁵¹

To obtain a realistic PES in which both the D_{3h} and C_{2v} seams are accurately modeled, a total of 421 grid points has been chosen to map the region defined by $4.000a_0 \leq Q_1 \leq 5.750a_0$ and $-0.040a_0 \leq Q_i (i = 2, 3) \leq 0.040a_0$. An extra 629 *ab initio* energies⁵⁰ have been considered, which amounts to a total of 1050 points used for the calibration process.

3 The DMBE I potential energy surface: a brief survey

The adiabatic ground-state PES reported elsewhere⁵⁰ for the $C_3(1^1A')$ radical assumes the following form:

$$V_I(\mathbf{R}) = V^{(1)} + V^{(2)}(\mathbf{R}) + V_{dc}^{(3)}(\mathbf{R}) + V_{I,EHF}^{(3)}(\mathbf{R}), \quad (2)$$

where, as usual,^{60–63} $V^{(1)}$ is a one-body term equal to the dissociation energy (D_e) of $C_2(a^3\Pi_u)$, $V^{(2)}(\mathbf{R})$ is the sum of the two-body potentials, and $V_{dc}^{(3)}(\mathbf{R})$ is the three-body dynamical correlation; see ref. 50 and ESI.† To ensure the proper cusp behavior,^{17,18} the three-body extended Hartree-Fock (EHF)

energy, $V_{I,EHF}^{(3)}(\mathbf{R})$, is expressed as a sum of two terms⁵⁰

$$V_{I,EHF}^{(3)}(\mathbf{R}) = V_{I,EHF}^{'(3)}(\mathbf{R}) + V_{I,EHF}^{''(3)}(\mathbf{R}), \quad (3)$$

where

$$V_{I,EHF}^{'(3)}(\mathbf{R}) = \left[P_1^{N'}(\Gamma_1, \Gamma_2, \Gamma_3) - \sqrt{\Gamma_2} P_2^{M'}(\Gamma_1, \Gamma_2, \Gamma_3) \right] T'_I(\mathbf{R}), \quad (4)$$

and

$$V_{I,EHF}^{''(3)}(\mathbf{R}) = \left[P_3^{N''}(\Gamma_1, \Gamma_2, \Gamma_3) - \Delta_1 \Delta_2 \Delta_3 P_4^{M''}(\Gamma_1, \Gamma_2, \Gamma_3) \right] T''_I(\mathbf{R}). \quad (5)$$

In eqn (4) and (5), $P_n^J(\Gamma_1, \Gamma_2, \Gamma_3)$ [$n = 1, \dots, 4$ and $J = N', M', N'', M''$] are polynomials of order J expressed as

$$P_n^J(\Gamma_1, \Gamma_2, \Gamma_3) = \sum_{i+2j+3k \leq J} c_{ijk}^n \Gamma_1^i \Gamma_2^j \Gamma_3^k, \quad (6)$$

where $\Gamma_1 = Q_1$, $\Gamma_2 = Q_2^2 + Q_3^2$, and $\Gamma_3 = Q_3(Q_3^2 - 3Q_2^2)$ define the integrity basis.⁶⁴ In turn, $T'_I(\mathbf{R})$ and $T''_I(\mathbf{R})$ are range-decaying factors.⁵⁰ As noted elsewhere,^{17,31,32,50} the polynomial in eqn (4) warrants that the DMBE form behaves as a linear function of the radial polar coordinate⁴ $\rho(Q_1) \equiv \sqrt{\Gamma_2} = \sqrt{Q_2^2 + Q_3^2}$ in the two dimensional branching plane [here denoted for a given value of Q_1 as $\mathbf{Q}_b(Q_1) = (Q_2, Q_3)$]. In turn, following ref. 17, the polynomials in eqn (5) provide the expected cusp behavior at C_{2v} degeneracies, which, in ref. 50, have been first modeled for a fixed valence angle of $\phi = 60.2128^\circ$. Thus, in eqn (5), Δ_c ($c = 1, 2$ and 3) are the distances (or the corresponding norms $\|\vec{\Delta}_c\|$ in Fig. 1) from any point in \mathbf{R} -space [say, $\vec{p} = (R_1, R_2, R_3)$] to the three permutationally equivalent C_{2v} crossing seams

$$\|\vec{\Delta}_1\| = \sqrt{\left[R_1 - t_0 \sqrt{2(1 - \cos \phi)} \right]^2 + (R_2 - t_0)^2 + (R_3 - t_0)^2} \quad (7)$$

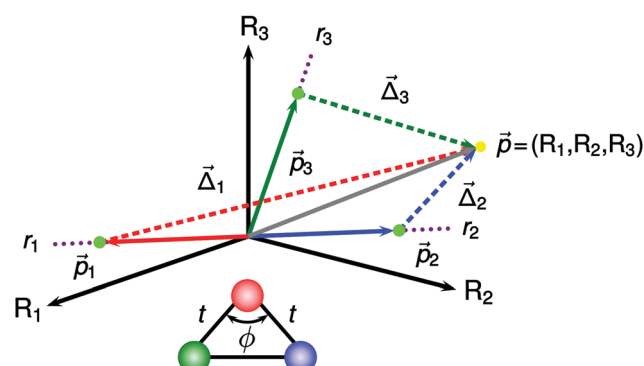


Fig. 1 Permutationally equivalent C_{2v} crossing seams for a fixed valence angle ϕ . The seams are shown as dots, with the distances from any point in \mathbf{R} -space (\vec{p} vector) to the corresponding crossing points (\vec{p}_1 , \vec{p}_2 and \vec{p}_3 vectors) indicated by the $\vec{\Delta}_1$, $\vec{\Delta}_2$ and $\vec{\Delta}_3$ vectors. The dummy variable t defines the associated parametric lines r_1 , r_2 and r_3 (see the text).

$$\|\vec{A}_2\| = \sqrt{(R_1 - t_0)^2 + [R_2 - t_0 \sqrt{2(1 - \cos \phi)}]^2 + (R_3 - t_0)^2} \quad (8)$$

$$\|\vec{A}_3\| = \sqrt{(R_1 - t_0)^2 + (R_2 - t_0)^2 + [R_3 - t_0 \sqrt{2(1 - \cos \phi)}]^2}, \quad (9)$$

where t_0 is the reference distance in $\vec{p}_1 = (t_0 \sqrt{2(1 - \cos \phi)}, t_0, t_0)$, $\vec{p}_2 = (t_0, t_0 \sqrt{2(1 - \cos \phi)}, t_0)$, and $\vec{p}_3 = (t_0, t_0, t_0 \sqrt{2(1 - \cos \phi)})$ along the parametric lines $r_1 = (t \sqrt{2(1 - \cos \phi)}, t, t)$, $r_2 = (t, t \sqrt{2(1 - \cos \phi)}, t)$, and $r_3 = (t, t, t \sqrt{2(1 - \cos \phi)})$; Fig. 1. Suffice it to add that t_0 is obtained from the requirement that \vec{A}_c is orthogonal to the seam, which is equivalent to solve $\vec{A}_c \cdot \vec{p}_c = 0$ for t_0 . This yields

$$t_0 = \frac{R_1 \sqrt{2(1 - \cos \phi)} + R_2 + R_3}{4 - 2 \cos \phi}, \quad (10)$$

for $\vec{A}_1 \cdot \vec{p}_1 = 0$, and

$$t_0 = \frac{R_1 + R_2 \sqrt{2(1 - \cos \phi)} + R_3}{4 - 2 \cos \phi} \quad (11)$$

$$t_0 = \frac{R_1 + R_2 + R_3 \sqrt{2(1 - \cos \phi)}}{4 - 2 \cos \phi}, \quad (12)$$

for $\vec{A}_2 \cdot \vec{p}_2 = 0$ and $\vec{A}_3 \cdot \vec{p}_3 = 0$, respectively; see elsewhere^{17,18} for details. Note that the parameters of eqn (4) and (5) have been obtained⁵⁰ from a fit to 629 scaled *ab initio* energies with a total unweighted root mean square deviation (rmsd) of 4.14 kJ mol⁻¹. It should be recalled that, unlike $V_{1,\text{EHF}}^{(3)}(\mathbf{R})$, $V_{1,\text{EHF}}^{\prime(3)}(\mathbf{R})$ in eqn (5) dies off Gaussian-like, and therefore is expected to be valid in a limited portion of configuration space, namely at the region defined by the minima of the C_{2v} crossings.^{17,50}

4 Modeling the C_{2v} disjoint seams

Consider the 2D branching plane $\mathbf{Q}_b(Q_1) = (Q_2, Q_3)$ in Fig. 2 defined by the coordinates Q_2 and Q_3 , for a fixed Q_1 . Clearly, $\forall Q_1$, $\mathbf{Q}_b(Q_1) = (0,0)$ defines equilateral triangular arrangements where the ground ($1^1\text{A}'$) and first excited ($2^1\text{A}'$) PESs of C_3 show a symmetry-dictated Ci.^{50,51} The C_{2v} crossing points are then defined by

$$\vec{p}_c' = (Q_2^c, Q_3^c) = (\rho_0 \cos(\varphi_c \pm n\pi), \rho_0 \sin(\varphi_c \pm n\pi)), \quad (13)$$

where the parametric dependences of $Q_2^c(Q_1)$, $Q_3^c(Q_1)$ and $\rho_0(Q_1)$ on Q_1 are eliminated thereof for convenience of notation. In turn, $\rho_0 = [(Q_2^c)^2 + (Q_3^c)^2]^{1/2}$ denotes the radius at which the three symmetry-equivalent disjoint seams are located with respect to the central Ci⁵¹ and φ_c ($c = 1, 2$ and 3) is the polar angle^{4,60,65} that explicitly defines the positions of the crossings; $\varphi_1 = \pi/2$, $\varphi_2 = 7\pi/6$ and $\varphi_3 = 11\pi/6$. In eqn (13), $n = 0$ or 1 is an integer that accounts for the proper rotation-in-plane of the C_{2v} seams on passing through the confluence point.⁵¹ Thus, the distance

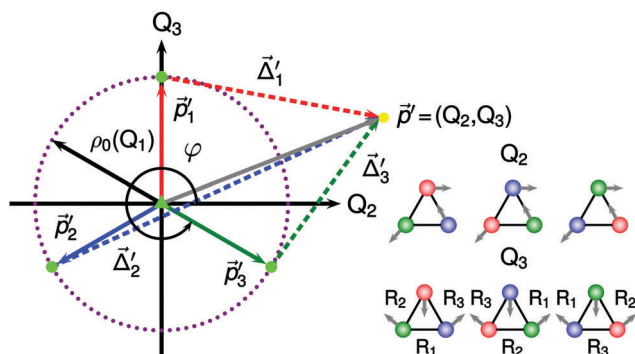


Fig. 2 Symmetry-equivalent C_{2v} crossing seams lying at $\varphi = \pi/2, 7\pi/6$ and $11\pi/6$ on a circle of radius $\rho_0(Q_1)$ in the (Q_2, Q_3) branching plane. Also shown at the origin, $(0,0)$, is the D_{3h} symmetry-required seam. The distances from any point in \mathbf{Q} -space (\vec{p}' vector) to the corresponding C_{2v} crossing points (\vec{p}_1' , \vec{p}_2' and \vec{p}_3' vectors) are indicated by the $\vec{\Delta}_1'$, $\vec{\Delta}_2'$ and $\vec{\Delta}_3'$ vectors.

from any point $\vec{p}' = (Q_2, Q_3)$ in \mathbf{Q} -space to the three permutationally equivalent C_{2v} crossing points (see Fig. 2) is defined by^{17,18}

$$\vec{A}_c' = \vec{p}' - \vec{p}_c' = (Q_2 - Q_2^c, Q_3 - Q_3^c) \quad (14)$$

and hence

$$\|\vec{A}_c'\| = \sqrt{(Q_2 - Q_2^c)^2 + (Q_3 - Q_3^c)^2}. \quad (15)$$

Thus, the only requirement to determine the norm $\|\vec{A}_c'\|$, and hence the cusp behavior of the adiabatic PESs, is to find the appropriate equation of the seam that relates the positions of the disjoint crossing points [Q_2^c, Q_3^c or ρ_0 ; see eqn (13)] and the size of the molecular triangle. In principle, such a requirement can be fulfilled by any type of well-behaved function of Q_1 . To accomplish this, we have performed *ab initio* calculations along $\mathbf{Q}_b(Q_1) = (0, Q_3)$ for different values of Q_1 ($4.000a_0 \leq Q_1 \leq 5.750a_0$). This allows us to determine the C_{2v} points of degeneracy between the $1^1\text{A}'$ and $2^1\text{A}'$ states along the line $(Q_2^1, Q_3^1) \equiv (0, Q_3^1)$; see Fig. 2. Various perspectives of the current results are illustrated in Fig. 3.

As shown in Fig. 3(a), the Cis at the C_{2v} symmetry occur not only for fixed valence angles of ref. 50 $\phi = 60.2128^\circ$, but also for angles varying between 59.7447° ($R = 3.324a_0$) and 60.9511° ($R = 2.298a_0$). Therefore, the crossing geometries lie in close proximity to the D_{3h} Ci ($\phi = 60.0^\circ$), with the valence angles deviating by less than 1.0° . Actually, as depicted in Fig. 3, such geometries ultimately coalesce with an equilateral triangular one at $R \approx 2.890a_0$ or $Q_1 \approx 5.005a_0$ (see Fig. 3) forming an intersection node or confluence of seams. In fact, following recent work¹⁷ for NO_2 (${}^1\text{A}''$), the equation of the seam could be well modeled in the \mathbf{R} -space by a straight line [Fig. 3(b)] of the form $R_1 = f(R) = a + bR$ where $R_2 = R_3 = R$, $a = 0.134a_0$ and $b = 0.954$; see elsewhere¹⁸ for generalizations employing non-linear functions. As shown, the errors in R_1 amount to $\approx 10^{-3}a_0$. However, the preliminary tests indicated that even such small deviations prevent an accurate fit of the proper C_{2v} cusp location in \mathbf{Q} -space, especially for geometries with stretched

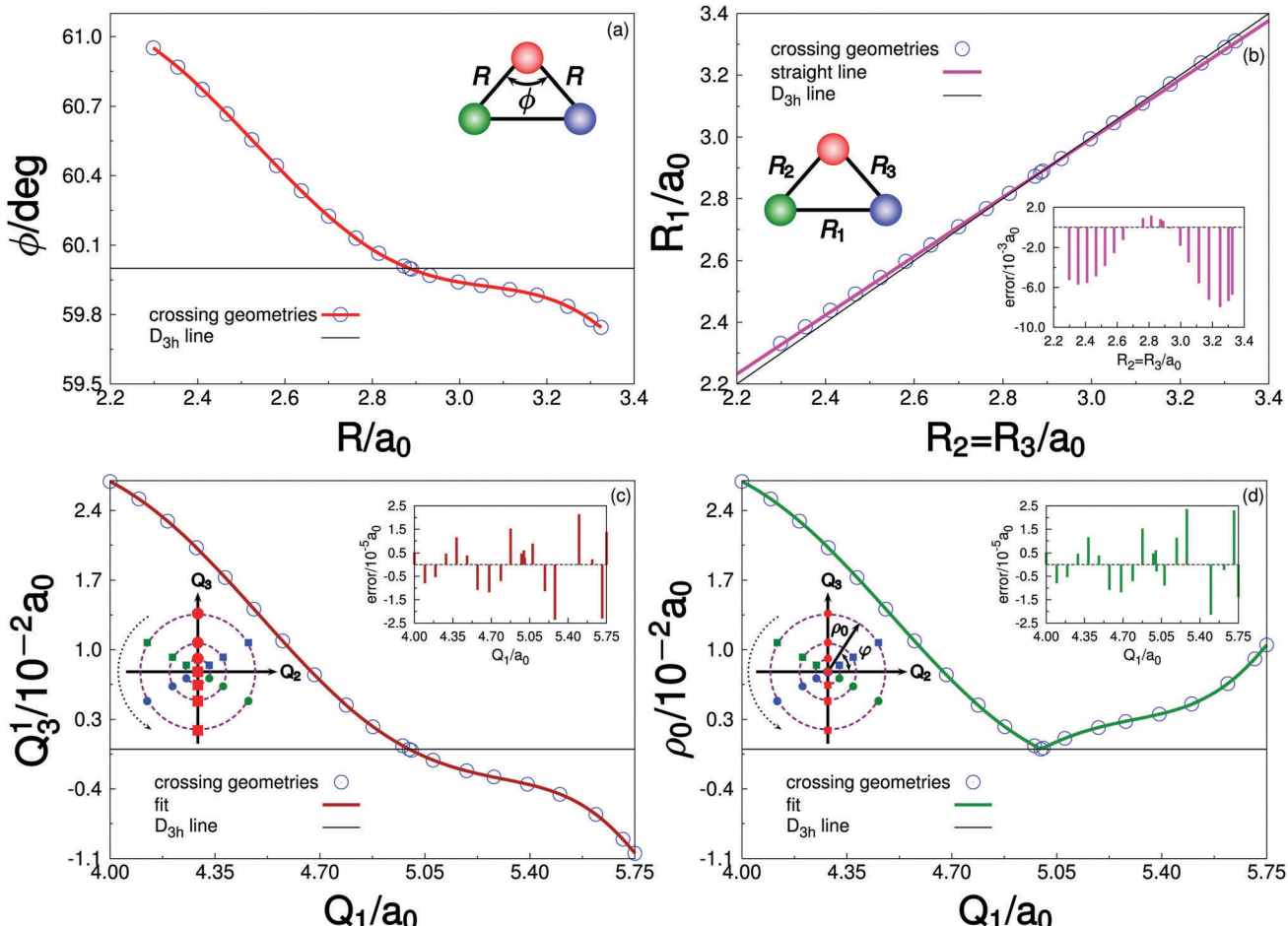


Fig. 3 Location of the C_{2v} crossing seam $(Q_2^1, Q_3^1) \equiv (0, Q_3^1)$ for distinct values of Q_1 . The seam is shown in different perspectives and coordinate systems: (a) in valence coordinates R and ϕ ; (b) in triangular coordinates R_1, R_2 and R_3 ; (c) Q_3^1 with respect to Q_1 [eqn (17)]; and (d) ρ_0 with respect to Q_1 [eqn (16)].

bond distances where the deviations from the simple straight line would be of the same order of magnitude as the difference between the geometries themselves [see the inset of Fig. 3(b)]. Thus, we have chosen an analytic form in ρ_0 that accurately mimics all C_{2v} crossing seams. This has been accomplished through a 1D fit of the various $(0, Q_3^1)$ crossing points obtained for each Q_1 , with ρ_0 extracted from the relation:

$$\rho_0 = |Q_3^1|. \quad (16)$$

As Fig. 3(c) shows, Q_3^1 can be accurately modeled by the form

$$Q_3^1 = \rho - \delta \tanh \left[\sum_{i=1}^5 \zeta_i (Q_1 - Q_1^0)^i \right], \quad (17)$$

which contains 8 adjustable parameters. Note that the linear fit in panel (b) deviates quite significantly from the points in panel (c) when plotted on the same scale (not shown for simplicity).

In fact, as seen in the inset of Fig. 3(c), the errors in the crossing geometries predicted by eqn (17) amount to $\approx 10^{-5} a_0$ at most. Clearly, the advantage of such a procedure, *i.e.*, fit Q_3^1 first and subsequently extract the associated radii from eqn (16), may circumvent problems with the analytic representation of the “cusp-like” behavior of ρ_0 near the intersection

node, as seen in Fig. 3(d). Note that the latter is predicted from the analytical form (17) to be located at $Q_1 = 4.997 a_0$. The numerical coefficients of eqn (17) are given as ESI.†

Once the value of ρ_0 is known, the distances to the three equivalent C_{2v} crossing seams $\Delta_1' \equiv \|\vec{\Delta}_1'\|$, $\Delta_2' \equiv \|\vec{\Delta}_2'\|$ and $\Delta_3' \equiv \|\vec{\Delta}_3'\|$ can then be determined from eqn (13)–(15). Note that, unlike ref. 17 and 18, no orthogonality relations between $\vec{\Delta}_c'$ and \vec{p}_c' , *i.e.*, $\vec{\Delta}_c' \cdot \vec{p}_c' = 0$, are needed here inasmuch as \vec{p}_c' is uniquely defined in the (Q_2, Q_3) plane and so will be $\|\vec{\Delta}_c'\|$.

In ref. 17 and 50, the desired cusp behavior on the adiabatic PESs has been accomplished by using the product of such distances [see eqn (5)] such as to ensure the permutational nature of the crossings. Clearly, as Fig. 4(a) shows, $-\Delta_1' \Delta_2' \Delta_3'$ behaves nonlinearly as one moves away from the intersection point. So, we define instead a set of symmetrized combinations of Δ_1' , Δ_2' and Δ_3' ,

$$\begin{pmatrix} S_1 \\ S_2 \\ S_3 \end{pmatrix} = \begin{pmatrix} \sqrt{1/3} & \sqrt{1/3} & \sqrt{1/3} \\ 0 & \sqrt{1/2} & -\sqrt{1/2} \\ \sqrt{2/3} & -\sqrt{1/6} & -\sqrt{1/6} \end{pmatrix} \begin{pmatrix} \Delta_1' \\ \Delta_2' \\ \Delta_3' \end{pmatrix}, \quad (18)$$

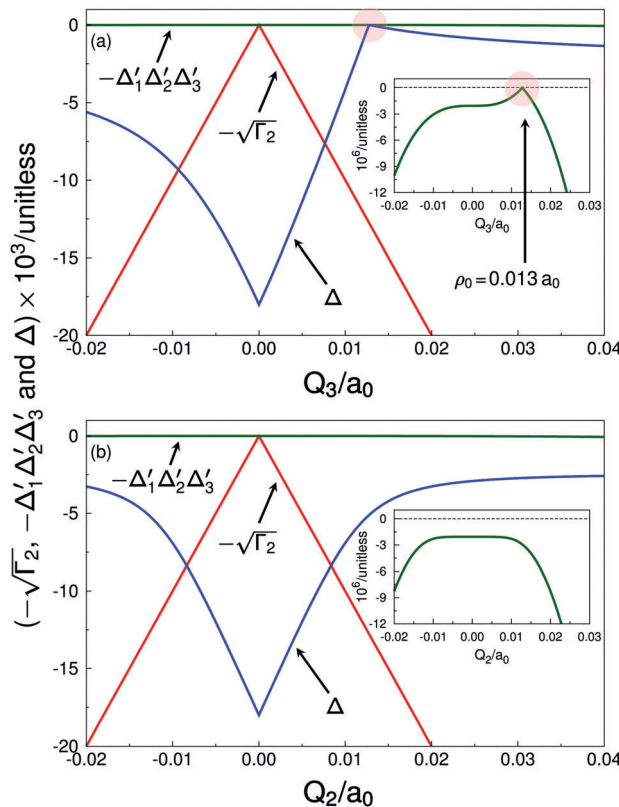


Fig. 4 Behavior of $-\sqrt{\Gamma_2}$, $-\Delta'_1 \Delta'_2 \Delta'_3$ and Δ along (a) the bending $[Q_b(Q_1) = (0, Q_3)]$; (b) asymmetric stretch $[Q_b(Q_1) = (Q_2, 0)]$ normal modes for $Q_1 = 4.520a_0$. The curve related to the Δ function is shifted by $-\sqrt{2}\rho_0$. Shaded red circles highlight the cusps at the C_{2v} symmetry.

and also

$$\Delta = \sqrt{S_2^2 + S_3^2}. \quad (19)$$

It is seen from Fig. 4 that Δ causes the desired cusps at the C_{2v} geometries. Needless to say, eqn (19) is analogous to the JT-type coordinate ($\sqrt{\Gamma_2}$), therefore yielding the proper linear dependence of the potential energy along the non-totally symmetric distortions. Note that Δ has built-in the permutational equivalency of the seams, thus allowing cusps to be created on adiabatic PESs of any X_3 -type system; see Fig. 5. This approach is here utilized to develop a novel DMBE form for $C_3(1^1A')$, thus ensuring the correct topological description of the 4 conical intersections. The details of the new analytical form employed here are discussed next.

5 The DMBE II potential energy surface

All terms in the novel PES have the same functional form as previously used,⁵⁰ with the exception of the three-body EHF term. Such a potential is then written as

$$V_{II}(\mathbf{R}) = V^{(1)} + V^{(2)}(\mathbf{R}) + V_{dc}^{(3)}(\mathbf{R}) + V_{II,EHF}^{(3)}(\mathbf{R}), \quad (20)$$

where $V^{(1)}$, $V^{(2)}(\mathbf{R})$, and $V_{dc}^{(3)}(\mathbf{R})$ assume the same meaning as in eqn (2); the details of the corresponding analytical forms are in

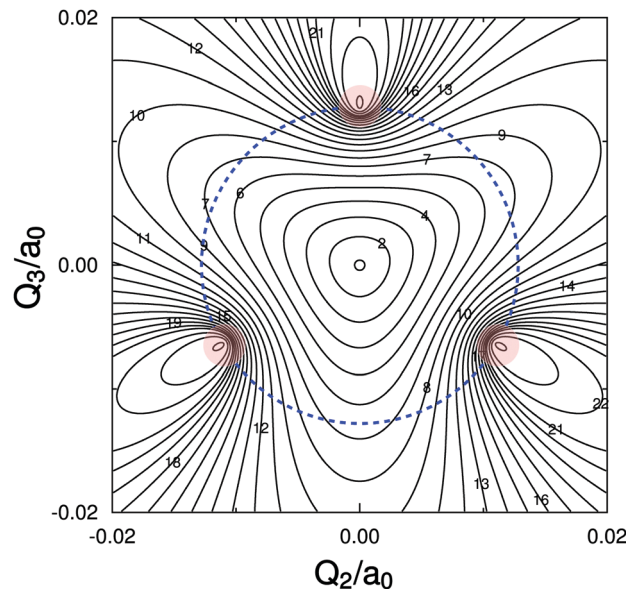


Fig. 5 Contour plot of Δ [eqn (19)] for $Q_1 = 4.520a_0$. As in Fig. 4, Δ is shifted by $-\sqrt{2}\rho_0$. Contours are equally spaced by 3.00×10^{-4} starting at -203.34×10^{-4} . Shaded red circles highlight the three C_{2v} symmetry-equivalent cusps.

ref. 50. In turn, the new three-body EHF component, $V_{II,EHF}^{(3)}(\mathbf{R})$, assumes the form

$$V_{II,EHF}^{(3)}(\mathbf{R}) = V'_{II,EHF}^{(3)}(\mathbf{R}) + V''_{II,EHF}^{(3)}(\mathbf{R}) + V'''_{II,EHF}^{(3)}(\mathbf{R}). \quad (21)$$

Note that, similarly to eqn (3), $V'_{II,EHF}^{(3)}(\mathbf{R})$ is the component that adequately describes the symmetry-imposed Ci at the D_{3h} symmetry, while the additional terms $V''_{II,EHF}^{(3)}(\mathbf{R})$ and $V'''_{II,EHF}^{(3)}(\mathbf{R})$ warrant the correct cusp behavior at C_{2v} degeneracies over the whole configuration space. They are given by

$$\begin{aligned} & V'_{II,EHF}^{(3)}(\mathbf{R}) \\ &= \left[P_1^{N'}(\Gamma_1, \Gamma_2, \Gamma_3) - \mathcal{F}_{nJT}(\mathbf{R}) \sqrt{\Gamma_2} P_2^{M'}(\Gamma_1, \Gamma_2, \Gamma_3) \right] T'_{II}(\mathbf{R}), \end{aligned} \quad (22)$$

$$\begin{aligned} & V''_{II,EHF}^{(3)}(\mathbf{R}) = \left[P_3^{N''}(\Gamma_1, \Gamma_2, \Gamma_3) - \mathcal{F}_{nJT}(\mathbf{R}) \sqrt{\Gamma_2} P_4^{M''}(\Gamma_1, \Gamma_2, \Gamma_3) \right. \\ & \quad \left. - \Delta P_5^{P''}(\Gamma_1, \Gamma_2, \Gamma_3) \right] T''_{II}(\mathbf{R}), \end{aligned} \quad (23)$$

and

$$\begin{aligned} & V'''_{II,EHF}^{(3)}(\mathbf{R}) = \left[P_6^{N'''}(\Gamma_1, \Gamma_2, \Gamma_3) - \mathcal{F}_{nJT}(\mathbf{R}) \sqrt{\Gamma_2} P_7^{M'''}(\Gamma_1, \Gamma_2, \Gamma_3) \right. \\ & \quad \left. - \Delta P_8^{P'''}(\Gamma_1, \Gamma_2, \Gamma_3) \right] T'''_{II}(\mathbf{R}). \end{aligned} \quad (24)$$

In eqn (22)–(24), $P_n^I(\Gamma_1, \Gamma_2 \text{ and } \Gamma_3)$ are polynomials that assume the same form as in eqn (6) and are suitably centered at the D_{3h} geometries with the bond lengths of R'_0 , R''_0 and R'''_0 , respectively. $T'_{II}(\mathbf{R})$, $T''_{II}(\mathbf{R})$ and $T'''_{II}(\mathbf{R})$ are range-determining

factors defined by

$$T'_{\text{II}}(\mathbf{R}) = \prod_{i=1}^3 \left\{ 1 - \tanh [\alpha' (R_i - R'_0)] \right\}, \quad (25)$$

$$\begin{aligned} T''_{\text{II}}(\mathbf{R}) = & \sum_{(i,j,k)} \left\{ \left\{ 1 - \tanh \left[\beta'' (R_i - R''_1) \right] \right\} \right. \\ & \left. \left\{ 1 - \tanh \left[\beta'' (R_j - R''_2) \right] \right\} \right. \\ & \left. \left\{ 1 - \tanh \left[\beta'' (R_k - R''_3) \right] \right\} \right\}, \end{aligned} \quad (26)$$

and

$$\begin{aligned} T'''_{\text{II}}(\mathbf{R}) = & \sum_{(i,j,k)} \left\{ \left\{ 1 - \tanh \left[\gamma''' (R_i - R'''_1) \right] \right\} \right. \\ & \left. \left\{ 1 - \tanh \left[\gamma''' (R_j - R'''_2) \right] \right\} \right. \\ & \left. \left\{ 1 - \tanh \left[\gamma''' (R_k - R'''_3) \right] \right\} \right\}, \end{aligned} \quad (27)$$

where the summations in eqn (26) and (27) extend over all possible cyclic permutations of (1, 2 and 3), and the symbols are defined later in the text.

As remarked elsewhere,^{49,51,54} at the confluence point between the D_{3h} and C_{2v} crossing seams (or, in other words, at the point where the three additional degeneracies coincide with the central one), the conical nature of the intersection is lost with the locus of degeneracy assuming the form of tangentially touching parabolas rather than cones placed apex to apex.⁵¹ Thence, in order to mimic such a topological feature, the JT-type coordinates of eqn (22)–(24) have all been multiplied by a “non-JT” factor

$$\mathcal{F}_{\text{nJT}}(\mathbf{R}) = 1 - \exp \{-\zeta [(R_1 - R_0^{\text{CP}})^2 + (R_2 - R_0^{\text{CP}})^2 + (R_3 - R_0^{\text{CP}})^2]\} \quad (28)$$

where $R_0^{\text{CP}} = 2.885a_0$ is the bond length of the confluence point predicted by the analytical function of eqn (17) with $\zeta = 1 \times 10^4 a_0^{-2}$ being the associated decaying parameter. Indeed, the $\mathcal{F}_{\text{nJT}}(\mathbf{R})$ term in eqn (28) guarantees that any singularity on the adiabatic PES due to $\sqrt{f_2}$ is cancelled out at such a point. Note that the Δ coordinate [eqn (19)] naturally vanishes at the intersection node, since $\rho_0 = 0$ [see Fig. 3(c) and (d)], $\Delta_1' = \Delta_2' = \Delta_3' = \|\vec{p}'\|$ and hence, $S_2 = S_3 = 0$; see eqn (13)–(19).

The strategy employed for the calibration of the $V'_{\text{II,EHF}}(\mathbf{R})$ term in eqn (21) is similar to the one used for the DMBE I PES,⁵⁰ and we summarize next only the basic approach. Following usual practice,^{60–63} the three-body EHF interaction energy for the extra set of 421 grid points was obtained by first removing, for a given triatomic geometry, the one-body [$V^{(1)}$] and the sum of the two-body energy terms [$V^{(2)}(\mathbf{R})$] from the corresponding *ab initio* DMBE-SEC interaction energy [defined with respect to the infinitely separated C(³P) atoms]. One then subtracts the dynamical correlation term [$V_{\text{dc}}^{(3)}(\mathbf{R})$] from the total three-body energy. It is the so calculated remaining energy that we adjust to the three-body polynomial form $V_{\text{II,EHF}}^{(3)}(\mathbf{R})$. Note that the same procedure has been adopted⁵⁰ in the calibration of the $V_{\text{I,EHF}}^{(3)}(\mathbf{R})$ term in eqn (3)

[previously denoted as $V_{\text{EHF}}^{(3)}(\mathbf{R})$]. For the fit, a version of the nonlinear Levenberg–Marquardt^{66,67} set of programs reported by Press *et al.*⁶⁸ has been used, with larger weights given to the most important regions of the PES, including the stationary points and the crossing geometries of the D_{3h} and C_{2v} symmetry.

As a first step in the least-squares fitting procedure, the parameters of the $V'_{\text{II,EHF}}^{(3)}(\mathbf{R})$ component [eqn (22)] have been kept fixed (including the non-linear ones) to those values reported in ref. 50, while allowing all the coefficients of the $V''_{\text{II,EHF}}^{(3)}(\mathbf{R})$ and $V'''_{\text{II,EHF}}^{(3)}(\mathbf{R})$ terms to vary (to these extra parameters, small initial guesses have been assigned). Note that the non-linear coefficients β'' , γ''' and ζ of eqn (26), (27) and (28), respectively, have been selected by a trial-and-error fit where the total rmsd is minimized. It should be emphasized at this point that the advantage of using such a double set of polynomials is to guarantee the continuation of the C_{2v} disjoint seams as one moves way from the corresponding MeX, an overall improvement over the DMBE I PES. Indeed, the $V'_{\text{II,EHF}}^{(3)}(\mathbf{R})$ and $V''_{\text{II,EHF}}^{(3)}(\mathbf{R})$ polynomials are centered at $Q_1 = 4.520a_0$ ($R'_0 = 2.610a_0$) and $Q_1 = 5.750a_0$ ($R''_0 = 3.320a_0$) with the range-functions $T''_{\text{II}}(\mathbf{R})$ and $T'''_{\text{II}}(\mathbf{R})$ defined with respect to the associated C_{2v} crossing geometries $R''_1 = 2620a_0$, $R''_2 = R''_3 = 2.604a_0$ and $R''_1 = 3.311a_0$, $R''_2 = R''_3 = 3.324a_0$, respectively.

Once a reasonable set of initial coefficients for the $V'_{\text{II,EHF}}^{(3)}(\mathbf{R})$ and $V''_{\text{II,EHF}}^{(3)}(\mathbf{R})$ terms has been generated, the second step consisted of relaxing all involved parameters. It turns out that this often yields solutions with unphysical features, notably in highly repulsive regions of the PES and structures with C_{2v} symmetries. In fact, this behavior should be expected due to the added flexibility in such a narrow region of the configuration space.⁷⁴ However, a smooth PES could be obtained by performing a series of constrained optimizations in which blocks of coefficients are floated while keeping the others fixed. Such a strategy was carried out until chemical accuracy (4.07 kJ mol⁻¹) was achieved. By employing such a procedure, all coefficients in eqn (22)–(24) [146 in total: 134 c_{ijk}^n , R'_0 , α' , R''_0 , β'' , R''_1 , $R''_2 = R''_3$, R''_0 , γ''' , R''_1 , $R''_2 = R''_3$, ζ and R_0^{CP}] have been determined from a fit to the 1050 *ab initio* points; the optimal numerical values are given as ESI.† The quality of the current fit may be judged from its stratified rmsd in Table 1. For comparison, we also give the corresponding rmsd obtained in DMBE I.⁵⁰ Accordingly, a good overall fit to the *ab initio* points has been achieved for the whole PES, notably in the regions containing the D_{3h} and C_{2v} crossing seams (typically, 135–490 kJ mol⁻¹ above the global minimum). As expected, the novel PES exhibits a similar accuracy to DMBE I in describing other relevant regions of the configuration space.

6 Features of the novel DMBE potential energy surface

The major features of the current DMBE PES are shown in Fig. 6–10, while the properties of the stationary points and

Table 1 Stratified rmsd, in kJ mol^{-1} , of the DMBE I and DMBE II PESs

Energy ^c	DMBE I ^a		DMBE II ^b	
	N ^d	rmsd	N ^d	rmsd
42	105	0.67	105	0.66
84	168	0.79	168	0.82
126	250	0.88	250	0.84
167	310	1.00	518	0.62
209	327	1.21	596	0.89
251	338	1.46	651	0.87
293	347	1.67	680	0.89
335	366	2.34	747	1.53
377	367	2.51	748	1.85
418	372	2.72	773	2.03
628	396	2.85	817	2.26
837	484	2.93	905	2.66
1255	572	3.56	993	3.14
1674	623	3.81	1044	3.70
2092	626	3.97	1047	3.90
2510	629	4.14	1050	4.07

^a Ref. 50. ^b This work. ^c The unit of energy is kJ mol^{-1} . Energy strata defined relative to the $C_3(1\Sigma_g^+)$ global minimum. ^d Number of calculated points up to indicated energy range.

other relevant structures are given in Table 2. Clearly, our approach allows an accurate description of both D_{3h} and C_{2v} crossing seams in the entire range of nuclear configuration space, a significant improvement over the previously reported PES.⁵⁰ As shown in Fig. 6, such a procedure has proven very effective in reducing the discrepancies between the *ab initio* data and the single-sheeted DMBE form of eqn (20) in the crossing regions. As noted elsewhere⁵¹ and depicted in Fig. 6 and 7, when the size of the molecular triangle increases (*i.e.*, from $Q_1 = 4.000a_0$ to $Q_1 \lesssim 4.997a_0$), the C_{2v} disjoint seams approach the symmetry-required D_{3h} Ci almost linearly and ultimately coalesce with the latter at $Q_1 = 4.997a_0$. In fact, as noted in Section 5 and seen from Fig. 7(c), at such a confluence

point, the quadratic nature of the PES is remarkable and the intersection appears to be a Renner–Teller-like^{49,51} rather than a conical one. This is a result of using the “non-JT” factor of eqn (28) in the three-body terms $V'_{\text{II,EHF}}(\mathbf{R})$, $V''_{\text{II,EHF}}(\mathbf{R})$ and $V'''_{\text{II,EHF}}(\mathbf{R})$ [eqn (22)–(24)]. Indeed, as shown in Fig. 6 and 7, any further increase of the perimeter leads to a rotation of the C_{2v} seams by $\pm\pi$ in the (Q_2, Q_3) -plane, thence becoming located at $Q_b(Q_1) = (0, -\rho_0)$, $(\sqrt{3}\rho_0/2, \rho_0/2)$, and $(-\sqrt{3}\rho_0/2, \rho_0/2)$.⁵¹ Clearly, this is accomplished by eqn (13) with the integer n being responsible for the shift of the disjoint seams when passing the confluence point.

The seam space¹ of the D_{3h} and C_{2v} symmetries is best visualized in Fig. 8, which depicts the continuously connected points of degeneracy for distinct values of Q_1 and Q_3 , respectively. Also shown are the *ab initio* crossing geometries highlighted in Fig. 6 as well as those obtained in ref. 50. Accordingly, the MeX for equilateral triangular arrangements (D_{3h}^{cusp}) is predicted to be located at $R_1 = R_2 = R_3 = 2.610a_0$ ($Q_1^{\text{cusp}} = 4.520a_0$) and lies $135.50 \text{ kJ mol}^{-1}$ above the linear global minimum (referred to as Min). As shown in Table 2, excellent agreement is found between such a structure and the one actually predicted from the DMBE I PES. In turn, the MeX for C_{2v} conformations (C_{2v}^{cusp}) shows characteristic bond lengths of $R_1 = 2.620a_0$ and $R_2 = R_3 = 2.604a_0$ [$Q_b(Q_1^{\text{cusp}}) = (0.013a_0)$ with $Q_1^{\text{cusp}} = 4.520a_0$], which lies $135.18 \text{ kJ mol}^{-1}$ higher in energy with respect to the Min structure. Note that two other symmetry-related MeXs of C_{2v} symmetry exist for similar cross-sections rotated by $\pm 2\pi/3$. Such structures are predicted to be located at $R_2 = 2.620a_0$, $R_1 = R_3 = 2.604a_0$ [$Q_b(Q_1^{\text{cusp}}) = (0.011a_0, -0.006a_0)$] and $R_3 = 2.620a_0$, $R_1 = R_2 = 2.604a_0$ [$Q_b(Q_1^{\text{cusp}}) = (-0.011a_0, -0.006a_0)$]. Note that the C_{2v}^{cusp} structure obtained here is also in excellent agreement with the corresponding MeX previously reported⁵⁰ with bond lengths and

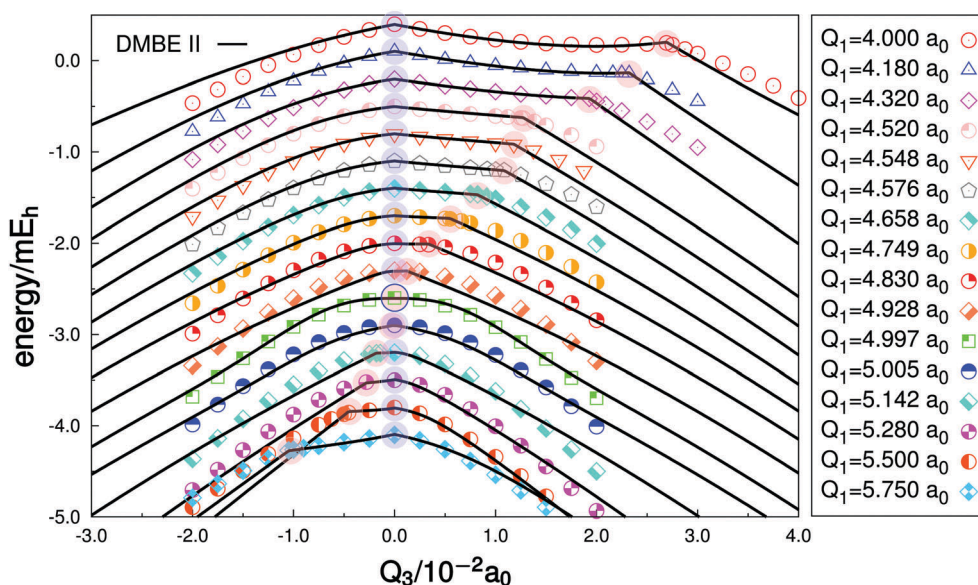


Fig. 6 Cross-sectional cuts of the DMBE II PES along Q_3 [$\mathbf{Q}_b(Q_1) = (0, Q_3)$] for different values of the symmetric stretching coordinate Q_1 ($4.000a_0 \leq Q_1 \leq 5.750a_0$). The dots indicate the DMBE-SEC points included in the fit of the present work. Energies are given with respect to the associated value at equilateral triangular geometries and shifted by multiples of $\pm 0.03mE_h$. Filled blue and red circles highlight the D_{3h} and C_{2v} crossing points, respectively.

Table 2 Properties of stationary points and other relevant structures on the $C_3(1^1A')$ DMBE PESs

	Method	R_1/a_0	R_2/a_0	R_3/a_0	$\Delta E/\text{kJ mol}^{-1}$	w_1/cm^{-1}	w_2/cm^{-1}	w_3/cm^{-1}
Min	DMBE II ^a	4.888	2.444	2.444	0 ^b	1203.9	61.0	2125.5
	DMBE I ^c	4.888	2.444	2.444	0	1204.2	63.5	2126.5
	Expt.	4.902	2.451	2.451 ^d	—	1224.49 ^e	63.42 ^e	2040.02 ^e
TS _{iso}	DMBE II	2.401	2.771	2.771	89.46	1295.2	1840.5	1047.3i
	DMBE I	2.399	2.768	2.768	89.58	1257.2	1873.3	1039.3i
SP ₂	DMBE II	2.478	5.511	5.511	795.35	1345.3	459.5i	546.5i
	DMBE I	2.477	5.509	5.509	795.04	1354.4	453.3i	542.7i
TS _{vdW}	DMBE II	2.470	7.249	7.249	755.80	1618.1	160.1	129.7i
	DMBE I	2.470	7.247	7.247	756.09	1613.1	160.0	136.7i
D_{3h}^{cusp}	DMBE II	2.610	2.610	2.610	135.50	—	—	—
	DMBE I	2.610	2.610	2.610	135.56	—	—	—
C_{2v}^{cusp}	DMBE II	2.620	2.604	2.604	135.18	—	—	—
	DMBE I	2.615	2.606	2.606	135.31	—	—	—

^a This work. ^b Relative to the $C_3(1^1\Sigma_g^+)$ global minimum. ^c Ref. 50. ^d Ref. 69. ^e Ref. 70 and 71. Separation between origin level and lowest $v_n = 1$ level.

^f Mixed theoretical/experimental approaches of ref. 72 and 73.

relative energy deviating by less than $0.005a_0$ and $-0.13 \text{ kJ mol}^{-1}$, respectively; see Table 2. It should be pointed out that the range of geometries considered here ($4.000a_0 \leq Q_1 \leq 5.750a_0$ and $-0.040a_0 \leq Q_i (i = 2, 3) \leq 0.040a_0$) is satisfactory to accurately mimic the C_{2v} disjoint seams at low-to-intermediate energy regimes of the adiabatic ground-state PES, typically up to $\approx 490 \text{ kJ mol}^{-1}$ above the $D_{\infty h}$ global minima; their validity range gets drastically limited by the extrapolation capability of the Q_3^1 function in eqn (17) as well as the range-determining factors $T''_{II}(\mathbf{R})$ and $T'''_{II}(\mathbf{R})$ [eqn (26) and (27)]. In fact, by decreasing the size of the equilateral triangle (e.g., for $Q_1 \ll 4.000a_0$), highly repulsive regions of the PES are accessible with both D_{3h} and C_{2v} crossing geometries ultimately coalescing to the $C(3^3P) + C(3^3P) + C(3^3P)$ united-(Ar)-atom limit; see Fig. 8 and 9. Of course, in such regions of the configuration space, the intrinsic accuracy of the *ab initio* calculations themselves is expected to be poor. Conversely, for $Q_1 \gg 5.750a_0$, the D_{3h} and C_{2v} crossing geometries collapse naturally into infinitely separated carbon atoms placed at the vertices of equilateral and isosceles triangles, respectively.

The global topography of the current DMBE PES is summarized in Fig. 9, which shows the C_{2v} insertion of a C atom into C_2 . Also shown in panel (b) are close views of the crossing regions illustrated in Fig. 6–8, together with the corresponding crossing geometries and representative degeneracy lines. Such a plot rationalizes in a comprehensive way all the relevant details. The most salient feature of Fig. 9(a), already remarked elsewhere,^{50,51,72,75,76} relates to the fact that the ground-state of C_3 shows its global minimum at $D_{\infty h}$ configurations with a characteristic bond length of $R_1/2 = R_2 = R_3 = 2.444a_0$. Such a structure matches the one predicted from the DMBE I PES with the harmonic vibrational frequencies deviating by -0.3 cm^{-1} , -2.5 cm^{-1} and -1.0 cm^{-1} for the symmetric (w_1), bending (w_2) and antisymmetric (w_3) motions, respectively.

Note that the Min structure arises from structural JT + PJT instabilities and distortions of the D_{3h}^{cusp} and C_{2v}^{cusp} MeXs toward a valence angle $\phi > 60.0$, with a stabilization energy of $135.18 \text{ kJ mol}^{-1}$ (with respect to C_{2v}^{cusp}). As seen in Fig. 9(b), if

displacements toward $\phi < 60.0$ take place, the title system attains the saddle point TS_{iso} with a stabilization energy of $46.04 \text{ kJ mol}^{-1}$. Such a structure (visible as a minimum in the 2D plot of Fig. 9) is therefore related to the isomerization between the three symmetry-equivalent C_3 global minima and is actually a transition state for pseudo-rotation.^{7–9} This is perhaps best seen from the plot shown later in Fig. 10. Note that, due to large contributions of the quadratic JT vibronic coupling constant G_E ,⁵¹ the associated minima (Min) are shifted away from the intersection region⁷⁷ as can be seen in Fig. 9(a) and 10. The classical barrier height for the isomerization process is $89.46 \text{ kJ mol}^{-1}$, which agrees well with the previously reported barrier of ref. 50 ($89.58 \text{ kJ mol}^{-1}$). Although the current PES predicts bond lengths and energy for TS_{iso} in reasonable agreement with the DMBE I form, the harmonic vibrational frequencies deviate by 38.0 cm^{-1} , -32.8 cm^{-1} and $8.0i \text{ cm}^{-1}$ for the symmetric (w_1), bending (w_2) and antisymmetric (w_3) motions, respectively; see Table 2. This is most likely due to the proximity of such a stationary point to the locus of intersections [see Fig. 9(b)] where small discrepancies between the current and previous fit are expected to manifest. In contrast, as shown in Table 2, in the regions of configuration space far away from the crossing seams, namely in the regions of the PES dominated by long range interactions, the properties of the stationary structures SP₂ and TS_{vdW} are essentially the same as those predicted⁵⁰ from DMBE I; for a detailed discussion of all stationary structures and the corresponding properties, see ref. 50. (Note that there is a missprint in ref. 50 concerning the subscript “vdW” in TS_{vdW}, which stands for “van der Waals”.)

As seen in the inset of Fig. 9(b), the novel DMBE PES obtained here provides not only an improvement in the description of the crossing region but also displays the expected sharp nature in the vicinity of the D_{3h} and C_{2v} crossing seams. This is a result of using the $\sqrt{T_2}$ and Δ coordinates. Because the present form guarantees by built-in construction the correct cusp behavior in an extended region of the nuclear

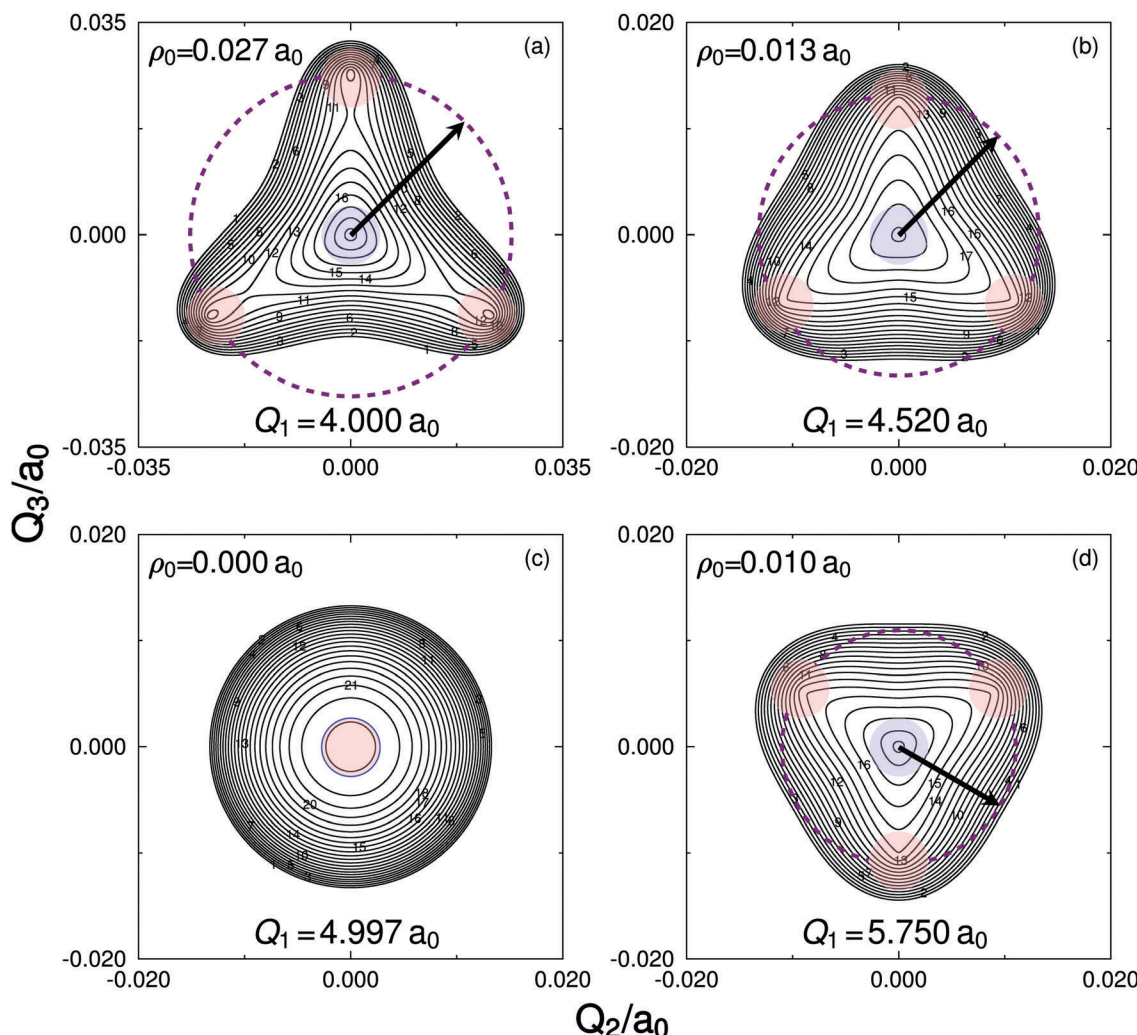


Fig. 7 Contour plots of the (Q_2, Q_3) -plane for fixed values of the Q_1 coordinate. (a) $Q_1 = 4.000 a_0$. Contours are equally spaced by $0.000025 E_h$ starting at $-0.1710 E_h$, (b) $Q_1 = 4.520 a_0$. Contours are equally spaced by $0.000015 E_h$ starting at $-0.2392 E_h$, (c) $Q_1 = 4.997 a_0$. Contours are equally spaced by $0.000012 E_h$ starting at $-0.2081 E_h$ and (d) $Q_1 = 5.750 a_0$. Contours are equally spaced by $0.000022 E_h$ starting at $-0.1048 E_h$. Filled blue and red circles highlight the D_{3h} and C_{2v} crossing points, respectively.

configuration space, one expects that the net GP effect is largely suppressed for any path in the (Q_2, Q_3) -plane that encircles the four singularity points. Obviously, no sign change is expected when looping around the confluence point in panel (c) of Fig. 7. Note that, in view of Fig. 9, the intersection node corresponds to the point in configuration space where the D_{3h} and C_{2v} intersection lines cross each other: $x = 2.885 a_0$ and $y = \sqrt{3}x/2 = 2.498 a_0$. Up to this point, the C_{2v} disjoint line lies below that of the D_{3h} symmetry, with the opposite being the case for regions above it; see Fig. 9(b).

The major topographical features of the DMBE II PES are best viewed in a relaxed triangular plot⁷⁸ using hyperspherical coordinates.¹⁵

$$\begin{pmatrix} Q \\ \beta \\ \gamma \end{pmatrix} = \begin{pmatrix} 1 & 1 & 1 \\ 0 & \sqrt{3} & -\sqrt{3} \\ 2 & -1 & -1 \end{pmatrix} \begin{pmatrix} R_1^2 \\ R_2^2 \\ R_3^2 \end{pmatrix}. \quad (29)$$

By relaxing the “size” Q of the molecular triangle so as to minimize the energy for fixed values of β and γ (or the “shape”), the scaled β^* and γ^* coordinates, plotted in Fig. 10, are given by⁷⁸

$$\beta^* = \beta/Q \quad (30)$$

$$\gamma^* = \gamma/Q. \quad (31)$$

As shown in Fig. 10(a), all the major topographical attributes of the current PES can be perceived through a close inspection of the line $\beta^* = 0$ and $\gamma^* \neq 0$ (the C_{2v} axis), with the associated symmetry-equivalent structures obtained for similar cuts rotated by $\pm 2\pi/3$. Note that linear geometries lie at the border of the physical circle, while the equilateral triangular conformation (D_{3h}) is located at the origin ($\beta^* = 0$ and $\gamma^* = 0$). Also shown in panels (b) and (c) are close views of the regions containing the three symmetry equivalent transition states TS_{iso} and $MeXs$, respectively. In addition to accurately reproducing the

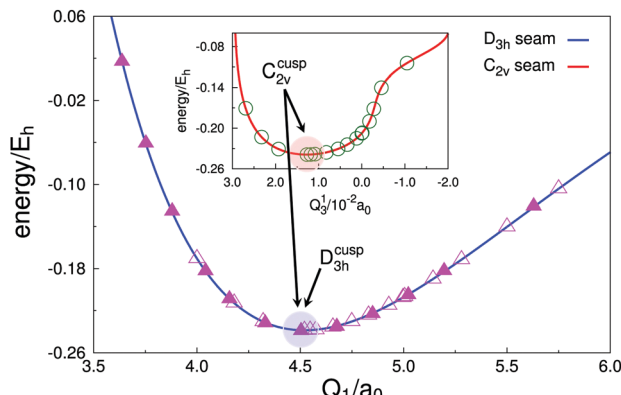


Fig. 8 Cuts along the D_{3h} and C_{2v} intersection lines as a function of Q_1 and Q_3 . The solid symbols correspond to the DMBE-SEC points calculated in ref. 50, while the open ones refer to the present work. Filled blue and red circles highlight the minimum energy crossing points at the D_{3h} and C_{2v} symmetries.

diatomic potentials, long-range forces at all asymptotic channels and valence interactions over the whole configuration space [already achieved by DMBE I⁵⁰], the novel DMBE II PES shows the correct topological behavior in the vicinity of the MeXs; see Fig. 10(c).

As shown in Fig. 10(c), the minima of the C_{2v} crossings lie at $\rho_0^* = 0.008a_0$, where ρ_0^* is the (scaled-) radial polar coordinate in the (β^*, γ^*) plane. Thence, on this circle of radius ρ_0^* in such a 2D plane, the four MeXs are uniquely defined by the coordinates $(0, 0)$, $(0, \rho_0^*)$, $(-\sqrt{3}\rho_0^*/2, -\rho_0^*/2)$ and $(\sqrt{3}\rho_0^*/2, -\rho_0^*/2)$. Note that the C_{2v}^{cusp} structures lie only 0.32 kJ mol⁻¹ below the corresponding MeX of the D_{3h} symmetry.

The probability of observing the GP effect (P_{GP}) may be speculated to be given by

$$P_{GP} \lesssim \frac{A_{ci}}{A_{tot}} \times 100 = (\rho_0^*)^2 \times 100 \quad (32)$$

where $A_{ci} = \pi(\rho_0^*)^2$ is the area of the circle defined by ρ_0^* , and $A_{tot} = \pi(\rho^*)^2$ with $\rho^* = 1$ is the radius of the physical circle in Fig. 10(a). For ground-state C_3 , this would yield $P_{GP} \lesssim 0.0064\%$, thus implying a very small number of paths that may sign-flip the electronic adiabatic wave function when looping an odd number of times the D_{3h} Ci.⁵¹ In most adiabatic energy regimes, one then expects the wave function to encircle the 4 Cis (classically, if having an energy above the barrier for pseudo-rotation) or not encircle any, which amounts basically to 100% of the cases.

7 Conclusions

A new single-sheeted DMBE II PES for ground-state $C_3(1^1A')$ has been reported. For this, we have suggested a form capable of accurately modeling the three symmetry-equivalent C_{2v} disjoint seams, in addition to the symmetry-required D_{3h} one, over the full configuration space. The present formalism warrants by

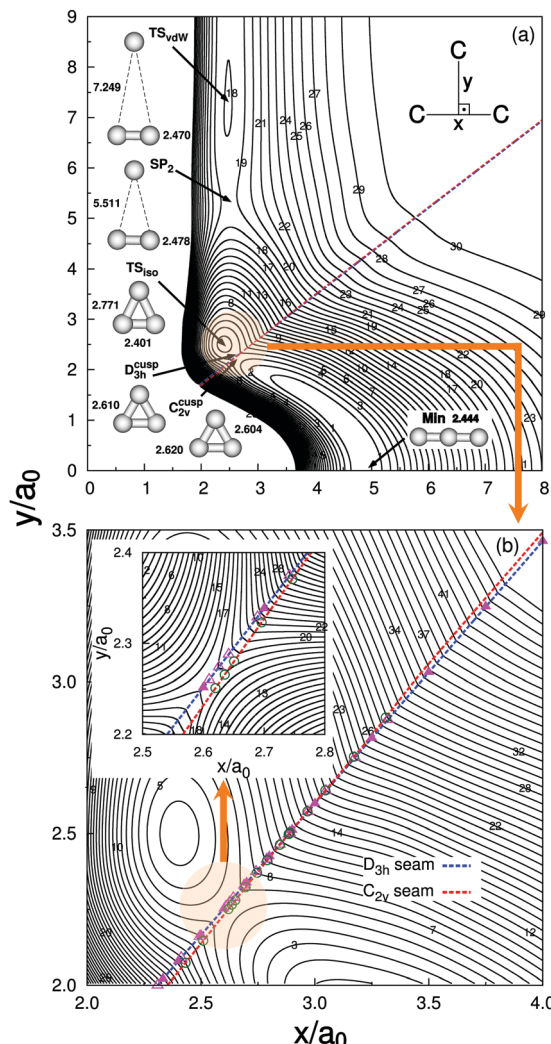


Fig. 9 Contour plots for the C_{2v} insertion of a C atom into the C_2 fragment. (a) Contours are equally spaced by $0.01E_h$ starting at $-0.2904E_h$. (b) Close view of the region defined by the D_{3h} and C_{2v} crossing seams. Contours are equally spaced by $0.004E_h$ starting at $-0.2800E_h$. In the inset of panel (b), contours are equally spaced by $0.0007E_h$ starting at $-0.2520E_h$. Key for *ab initio* crossing points as in Fig. 8.

built-in construction the confluence of the above crossings and the change-in-phase of the C_{2v} seams when the size of the molecular perimeter fluctuates. Up to 1050 *ab initio* energies have been employed in the calibration procedure, of which 421 were used to map the loci of intersections. The calculated energies have been scaled to account for the incompleteness of the basis set and truncation of the MRCI expansion and fitted analytically with chemical accuracy. The novel DMBE form is shown to accurately mimic the region defined by the 4 Cis, while exhibiting attributes similar to the ones predicted from the previously reported DMBE I PES in the regions away from the crossing seams. Despite focusing on C_3 , the present approach should be applicable to any adiabatic PES of X_3 -type systems experiencing similar topological effects, in particular for so-called small linear parameter JT molecules.

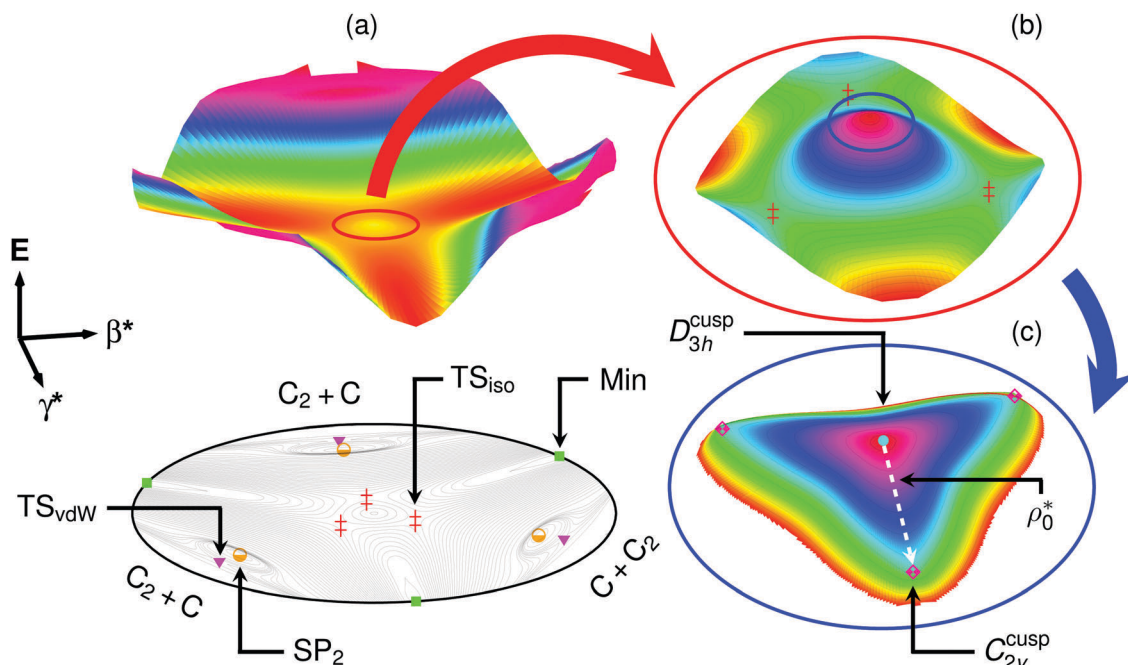


Fig. 10 Relaxed triangular plot in hyperspherical coordinates depicting the location and symmetry of all stationary points and other relevant structures discussed in the present work for the ground state of C_3 . (a) Contours are equally spaced by $0.005E_h$ starting at $-0.2904E_h$. (b) Close view of the region defined by the three symmetry related TS_{iso} structures and delimited by the bold red circle. Contours are equally spaced by $0.001E_h$ starting at $-0.2700E_h$. (c) Close view of the conical intersection region showing the minimum of the crossing seam at the D_{3h} symmetry as well as the minimum of the three equivalent symmetry related C_{2v} crossing points (inside the bold blue circle). Contours are equally spaced by $0.00002E_h$ starting at $-0.2390E_h$.

Conflicts of interest

There are no conflicts to declare.

Acknowledgements

This work was supported by Fundação para a Ciência e a Tecnologia and Coimbra Chemistry Centre, Portugal, through the project POCI-01-0145-FEDER-007630. C. M. thanks also the CAPES Foundation (Ministry of Education of Brazil) for a scholarship (Process BEX 0417/13-0).

References

- 1 W. Domcke, D. R. Yarkony and H. Köppel, *Conical Intersections: Electronic Structure, Dynamics & Spectroscopy*, World Scientific Publishing, Singapore, 2004, vol. 15.
- 2 G. J. Atchity, S. S. Xantheas and K. Ruedenberg, *J. Chem. Phys.*, 1991, **95**, 1862–1876.
- 3 D. R. Yarkony, *Acc. Chem. Res.*, 1998, **31**, 511–518.
- 4 A. J. C. Varandas, *Chem. Phys. Lett.*, 2010, **487**, 139–146.
- 5 H. A. Jahn and E. Teller, *Proc. R. Soc. London, Ser. A*, 1937, **161**, 220–235.
- 6 R. Englman, *The Jahn-Teller Effect*, John Wiley & Sons, New York, 1973.
- 7 I. B. Bersuker and V. Z. Polinger, *Vibronic Interactions in Molecules and Crystals*, Springer-Verlag, Berlin, 1989.
- 8 I. B. Bersuker, *The Jahn-Teller Effect*, Cambridge University Press, Cambridge, 2006.
- 9 I. B. Bersuker, *Chem. Rev.*, 2001, **101**, 1067–1114.
- 10 D. R. Yarkony, *Chem. Rev.*, 2012, **112**, 481–498.
- 11 J. von Neumann and E. P. Wigner, *Phys. Z.*, 1929, **30**, 467–470.
- 12 E. Teller, *J. Phys. Chem.*, 1937, **41**, 109–116.
- 13 G. Herzberg and H. C. Longuet-Higgins, *Discuss. Faraday Soc.*, 1963, **35**, 77–82.
- 14 H. C. Longuet-Higgins, *Proc. R. Soc. London, Ser. A*, 1975, **344**, 147–156.
- 15 C. A. Mead and D. G. Truhlar, *J. Chem. Phys.*, 1979, **70**, 2284–2296.
- 16 M. V. Berry, *Proc. R. Soc. London, Ser. A*, 1984, **392**, 45–57.
- 17 B. R. L. Galvão, V. C. Mota and A. J. C. Varandas, *J. Phys. Chem. A*, 2015, **119**, 1415–1421.
- 18 B. R. L. Galvão, V. C. Mota and A. J. C. Varandas, *Chem. Phys. Lett.*, 2016, **660**, 55–59.
- 19 M. Born and R. Oppenheimer, *Ann. Phys.*, 1927, **389**, 457–484.
- 20 M. Born and K. Huang, *Dynamical Theory of Crystal Lattices*, Oxford, Clarendon Press, 1954.
- 21 C. A. Mead and D. G. Truhlar, *J. Chem. Phys.*, 1982, **77**, 6090–6098.
- 22 J. N. Murrell, S. Carter, S. C. Farantos, P. Huxley and A. J. C. Varandas, *Molecular Potential Energy Functions*, John Wiley & Sons, Chichester, 1984.
- 23 T. Pacher, L. S. Cederbaum and H. Köppel, *Adv. Chem. Phys.*, 1993, **87**, 293–391.
- 24 J. G. Atchity and K. Ruedenberg, *Theor. Chem. Acc.*, 1997, **97**, 47–58.

- 25 A. J. Doblyn and P. J. Knowles, *Mol. Phys.*, 1997, **91**, 1107–1124.
- 26 A. Thiel and H. Köppel, *J. Chem. Phys.*, 1999, **110**, 9371–9383.
- 27 V. C. Mota and A. J. C. Varandas, *J. Phys. Chem. A*, 2008, **112**, 3768–3786.
- 28 A. J. C. Varandas, *J. Chem. Phys.*, 2008, **129**, 234103.
- 29 A. J. C. Varandas, *Chem. Phys. Lett.*, 2009, **471**, 315–321.
- 30 B. R. L. Galvão, P. J. S. B. Caridade and A. J. C. Varandas, *J. Chem. Phys.*, 2012, **137**, 22A515.
- 31 A. J. C. Varandas and J. N. Murrell, *Faraday Discuss. Chem. Soc.*, 1977, **62**, 92–109.
- 32 R. N. Porter, R. M. Stevens and M. Karplus, *J. Chem. Phys.*, 1968, **49**, 5163–5178.
- 33 A. J. C. Varandas, F. B. Brown, C. A. Mead, D. G. Truhlar and N. C. Blais, *J. Chem. Phys.*, 1987, **86**, 6258–6269.
- 34 M. Cernei, A. Alijah and A. J. C. Varandas, *J. Chem. Phys.*, 2003, **118**, 2637–2646.
- 35 L. P. Viegas, M. Cernei, A. Alijah and A. J. C. Varandas, *J. Chem. Phys.*, 2004, **120**, 253–259.
- 36 A. J. C. Varandas, A. Alijah and M. Cernei, *Chem. Phys.*, 2005, **308**, 285–295.
- 37 B. R. L. Galvão and A. J. C. Varandas, *J. Phys. Chem. A*, 2011, **115**, 12390–12398.
- 38 V. C. Mota, P. J. S. B. Caridade and A. J. C. Varandas, *Int. J. Quantum Chem.*, 2011, **111**, 3776–3785.
- 39 V. C. Mota, P. J. S. B. Caridade and A. J. C. Varandas, *J. Phys. Chem. A*, 2012, **116**, 3023–3034.
- 40 V. C. Mota and A. J. C. Varandas, *J. Phys. Chem. A*, 2007, **111**, 10191–10195.
- 41 J. W. Zwanziger and E. R. Grant, *J. Chem. Phys.*, 1987, **87**, 2954–2964.
- 42 H. Koizumi and I. B. Bersuker, *Phys. Rev. Lett.*, 1999, **83**, 3009–3012.
- 43 H. Köppel and R. Meiswinkel, *Z. Phys. D: At., Mol. Clusters*, 1994, **32**, 153–156.
- 44 R. G. Sadygov and D. R. Yarkony, *J. Chem. Phys.*, 1999, **110**, 3639–3642.
- 45 D. R. Yarkony, *J. Chem. Phys.*, 1999, **111**, 4906–4912.
- 46 S. Mukherjee, S. Bandyopadhyay, A. K. Paul and S. Adhikari, *J. Phys. Chem. A*, 2013, **117**, 3475–3495.
- 47 S. Mukherjee and S. Adhikari, *Chem. Phys.*, 2014, **440**, 106–118.
- 48 P. Garcia-Fernandez, I. B. Bersuker and J. E. Boggs, *J. Chem. Phys.*, 2006, **125**, 104102.
- 49 J. J. Dillon and D. R. Yarkony, *J. Chem. Phys.*, 2007, **126**, 124113.
- 50 C. M. R. Rocha and A. J. C. Varandas, *J. Chem. Phys.*, 2015, **143**, 074302.
- 51 C. M. R. Rocha and A. J. C. Varandas, *J. Chem. Phys.*, 2016, **144**, 064309.
- 52 G. J. Atchity and K. Ruedenberg, *J. Chem. Phys.*, 1999, **110**, 4208–4212.
- 53 D. R. Yarkony, *Theor. Chem. Acc.*, 1998, **98**, 197–201.
- 54 S. Matsika and D. R. Yarkony, *J. Phys. Chem. A*, 2002, **106**, 2580–2591.
- 55 P. G. Szalay, T. Müller, G. Gidofalvi, H. Lischka and R. Shepard, *Chem. Rev.*, 2012, **112**, 108–181.
- 56 T. H. Dunning, *J. Chem. Phys.*, 1989, **90**, 1007–1023.
- 57 R. A. Kendall, T. H. Dunning and R. J. Harrison, *J. Chem. Phys.*, 1992, **96**, 6796–6806.
- 58 H. J. Werner, P. J. Knowles, G. Knizia, F. R. Manby and M. Schütz *et al.*, *MOLPRO, a package of ab initio programs, version 2010.1*, Cardiff, UK, 2010, see: <http://www.molpro.net>.
- 59 A. J. C. Varandas, *J. Chem. Phys.*, 1989, **90**, 4379–4391.
- 60 A. J. C. Varandas, *Adv. Chem. Phys.*, 1988, **74**, 255–338.
- 61 A. J. C. Varandas, *THEOCHEM*, 1985, **120**, 401–424.
- 62 A. J. C. Varandas, in *Reaction and Molecular Dynamics*, ed. A. Laganà and A. Riganelli, Springer, Berlin Heidelberg, 2000, vol. 75, pp. 33–56.
- 63 A. J. C. Varandas, in *Conical Intersections: Electronic Structure, Dynamics & Spectroscopy*, ed. W. Domcke, D. R. Yarkony and H. Köppel, World Scientific, 2004, vol. 15, ch. 5, pp. 205–270.
- 64 A. J. C. Varandas and J. N. Murrell, *Chem. Phys. Lett.*, 1981, **84**, 440–445.
- 65 A. J. C. Varandas, J. Tennyson and J. N. Murrell, *Chem. Phys. Lett.*, 1979, **61**, 431–434.
- 66 K. Levenberg, *Q. Appl. Math.*, 1944, **2**, 164–168.
- 67 D. W. Marquardt, *SIAM J. Appl. Math.*, 1963, **11**, 431–441.
- 68 W. H. Press, S. A. Teukolsky, W. T. Vetterling and B. P. Flannery, *Numerical Recipes in Fortran: The Art of Scientific Computing*, Cambridge University Press, New York, NY, USA, 2nd edn, 1993.
- 69 K. W. Hinkle, J. J. Keady and P. F. Bernath, *Science*, 1988, **241**, 1319–1322.
- 70 G. Zhang, K. Chen, A. J. Merer, Y. Hsu, W. Chen, S. Shaji and Y. Liao, *J. Chem. Phys.*, 2005, **122**, 244308.
- 71 J. Krieg, V. Lutter, C. P. Endres, I. H. Keppeler, P. Jensen, M. E. Harding, J. Vázquez, S. Schlemmer, T. F. Giesen and S. Thorwirth, *J. Phys. Chem. A*, 2013, **117**, 3332–3339.
- 72 B. Schröder and P. Sebald, *J. Chem. Phys.*, 2016, **144**, 044307.
- 73 A. A. Breier, T. Büchling, R. Schnierer, V. Lutter, G. W. Fuchs, K. M. T. Yamada, B. Mookerjea, J. Stutzki and T. F. Giesen, *J. Chem. Phys.*, 2016, **145**, 234302.
- 74 A. J. C. Varandas, *J. Chem. Phys.*, 2013, **138**, 054120.
- 75 M. Mladenović, S. Schmatz and P. Botschwina, *J. Chem. Phys.*, 1994, **101**, 5891–5899.
- 76 K. Ahmed, G. G. Balint-Kurti and C. M. Western, *J. Chem. Phys.*, 2004, **121**, 10041–10051.
- 77 T. A. Barckholtz and T. A. Miller, *Int. Rev. Phys. Chem.*, 1998, **17**, 435–524.
- 78 A. J. C. Varandas, *Chem. Phys. Lett.*, 1987, **138**, 455–461.